

# Catadioptric hyperspectral imaging, an unmixing approach

ISSN 1751-9632  
 Received on 15th October 2019  
 Revised 8th April 2020  
 Accepted on 11th May 2020  
 E-First on 14th October 2020  
 doi: 10.1049/iet-cvi.2019.0784  
 www.ietdl.org

Didem Ozisik Baskurt<sup>1</sup> ✉, Yalin Bastanlar<sup>2</sup>, Yasemin Yardimci Cetin<sup>1</sup>

<sup>1</sup>METU Informatics Institute, Universiteler Mahallesi, Dumlupınar Bulvarı, No:1, 06800, Ankara, Turkey

<sup>2</sup>Computer Engineering Department, IZTECH, Gulbahce, 35430 Urla, Izmir, Turkey

✉ E-mail: didemozisik@gmail.com

**Abstract:** Hyperspectral imaging systems provide dense spectral information on the scene under investigation by collecting data from a high number of contiguous bands of the electromagnetic spectrum. The low spatial resolutions of these sensors frequently give rise to the mixing problem in remote sensing applications. Several unmixing approaches are developed in order to handle the challenging mixing problem on perspective images. On the other hand, omnidirectional imaging systems provide a 360-degree field of view in a single image at the expense of lower spatial resolution. In this study, we propose a novel imaging system which integrates hyperspectral cameras with mirrors so on to yield catadioptric omnidirectional imaging systems to benefit from the advantages of both modes. Catadioptric images, incorporating a camera with a reflecting device, introduce radial warping depending on the structure of the mirror used in the system. This warping causes a non-uniformity in the spatial resolution which further complicates the unmixing problem. In this context, a novel spatial-contextual unmixing algorithm specifically for the large field of view of the hyperspectral imaging system is developed. The proposed algorithm is evaluated on various real-world and simulated cases. The experimental results show that the proposed approach outperforms compared methods.

## 1 Introduction

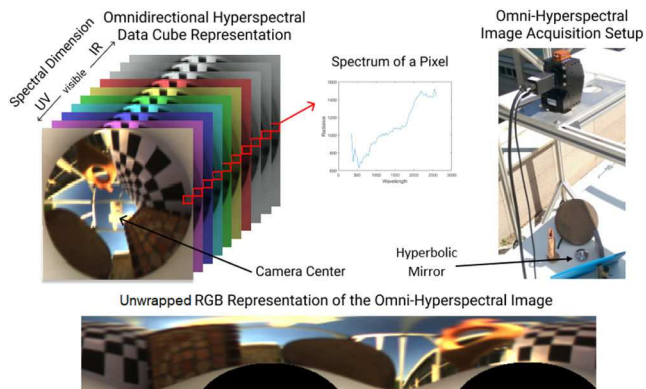
Hyperspectral data analysis attracts the interest of researchers working in the fields of computer vision and remote sensing, because it provides dense spectral information about the material to be monitored. Remote sensing applications aim to monitor large observation fields in a rapid way with a non-destructive manner. The existing studies on remote sensing and hyperspectral imaging applications, utilise the platforms which are mostly mounted on airborne or unmanned air vehicles (UAVs) in order to monitor large areas. However, airborne platforms have operational difficulties such as inappropriate weather conditions, flight permissions, no fly zones and costly aircraft hire. In addition, UAVs have limitations on the load of the imaging system containing heavy imaging hardware such as sensor and processing unit. In this study, we aim to increase field of view (FOV) of traditional hyperspectral imaging systems which use lenses having narrow FOV. Therefore, we contribute to existing hyperspectral and multispectral imaging systems with providing a large FOV. Fish-eye lenses, stitching several images captured by a narrow FOV camera and catadioptric systems are examples for large FOV imaging systems. Catadioptric cameras are the optical systems in which refraction (lenses) and reflection (mirrors) are combined. While these systems produce a deformation in the structure of the image due to the convex mirror used in the system, they are able to present 360 degree FOV in the horizontal plane. The term omnidirectional is used to denote that the light rays from all directions are collected. In our work, we aim to benefit from hyperspectral imaging and omnidirectional imaging technologies to obtain a catadioptric omnidirectional hyperspectral camera, and to handle the issues arising due to combining these technologies. There are very few reported studies which use high spectral information for omnidirectional imaging. These studies are summarised in Section 2. The low spatial resolution of the sensors frequently bring about the mixing problem in hyperspectral imaging applications. Several unmixing approaches are developed in order to handle the challenging mixing problem on perspective images. To our knowledge ours is the first study that investigates the applicability of unmixing algorithms for omnidirectional

hyperspectral images. We propose capturing a single omnidirectional image without requiring a prior stitching step.

The performance of the image processing algorithms, the robustness of the results and the detailed information provided by the sensors are highly dependent on the increased spectral and spatial resolution of the data. The conventional hyperspectral imagers renounce the high spatial resolution in favour of the high spectral resolution. Today's remote sensing technology on satellite and airborne applications is limited with the constraints: data storage capacity, the transmittance broadband between the imager and ground station, the weight limit to be carried on [1]. These constraints cause to have a lower spatial resolution which remains incapable of imaging the object to be analysed. In this case, the pixels captured in such scenario may not purely contain a single material. The pixel signature is mixed of the spectral signatures of the objects which are in the scene that are spatially covered by the pixel. At that point, a sub-pixel level analysis is needed, and this wide research area is termed as spectral unmixing. Additionally, the pure spectral signatures of the materials which exist in the scene, are called as endmembers.

The catadioptric hyperspectral image analysis requires different unmixing approaches compared to the traditional hyperspectral image analysis. In this study, some improvements specific to the catadioptric images on unmixing algorithms are proposed. Although we present a case which uses a catadioptric imaging system, our proposed method is applicable to all systems where a spatial non-uniformity occurs. This could be from any three-dimensional (3D) scene for which the near field object resolution is higher than that of the far field as in the case of perspective cameras. As will be given in Section 2, several recent publications indicate an interest in omnidirectional hyperspectral systems and these systems are of interest in their own right. In principle the proposed system can be applied to all hyperspectral cameras but the mirror that is attached to the camera should be an effective reflector for the spectral band sensed by the camera. In our case, we had a stainless steel reflector that has a steady spectral response in the VNIR region.

The proposed methods in this study are based on the spatial resolution of the pixels. Therefore, the literature works on



**Fig. 1** Proposed omnidirectional hyperspectral imaging system consists of a convex (hyperboloidal) mirror and a hyperspectral camera looking at the mirror

catadioptric image formation are analysed in depth. These studies enable us to compute the spatial resolution factor of each pixel in the scene, and consequently, to generate a map that illustrates the change on the spatial resolution values.

The first proposed improvement is for integrating the spatial resolution difference into the geometrical and spatial-contextual unmixing methods. We also theoretically examined the contribution of implementing the spatial resolution map into unmixing algorithms. Another improvement is proposed for geometrical unmixing approaches. We propose to rate the pixels in the convex structure according to their spatial resolution factors. The last novel improvement proposed in this study is a local spectral mixing analysis approach. In the proposed method, we divide the scene according to the catadioptric image formation.

The study is organised as follows: Section 2 introduces the basic concepts, advantages, constraints and application areas of both technology: hyperspectral imaging and omnidirectional imaging. Section 3.1 gives a simple introduction to catadioptric imaging principles. We also investigate the spectral characteristic of the mirror used in the omnidirectional imaging. Section 3.2 provides the details of spatial resolution in a catadioptric system. Section 3.3 provides information about the unmixing problem, and state-of-the-art algorithms. Section 4 includes the novel approaches specially investigated for the proposed omnidirectional hyperspectral imaging system. The evaluation of the proposed methods is given in Section 5. The comparison of the methods with the state-of-the-art algorithms are also shared in that section.

The source code and the catadioptric hyperspectral data set acquired in this study is shared on <https://github.com/bdidem/Catadioptric-Hyperspectral-Imaging-An-Unmixing-Approach.git>, as our contribution to the community.

## 2 Related work

A 3D hyperspectral data cube is obtained by measuring the spectral signature of each pixel. While the first two dimensions represent the spatial domain of the scene, the third dimension represents the data gathered from each spectral band. Hyperspectral imagery is preferred in a wide array of remote sensing applications. Improvements in sensor technologies enable to lower costs and weight, and make the use of sensor more practical. The proposed omnidirectional hyperspectral imaging system is illustrated in Fig. 1. The system is composed of a hyperspectral camera and a hyperboloidal mirror, which makes it a catadioptric omnidirectional camera. The scheme demonstrates a representation of an omnidirectional hyperspectral data cube. It also shows a signature gathered from a pixel in the data cube. A sample omni-hyperspectral image acquisition setup is shown in the figure. Finally, an unwrapped visualisation of the omnidirectional image is given in the scheme.

As catadioptric systems can be composed of many planar mirrors [2], they can also benefit from single curved mirrors, where paraboloidal and hyperboloidal mirrors are the most popular ones. In this study we focus on catadioptric systems with a single mirror.

The study in [3] briefly explains single-viewpoint property of catadioptric systems. The light rays coming from the scene and targeting the focal point (single viewpoint) of the hyperboloidal mirror are reflected on the mirror surface so that they pass through the pinhole (camera centre). On the other hand, paraboloidal mirrors reflect the rays orthogonally and that's why they require the use of a telecentric lens to collect the parallel rays.

The application areas such as surveillance and simultaneous localisation and mapping highly need a system that is easy to use, and captures wide FOV in a single image. Thus, it enables fast analysis of the scene without need the installment of several cameras with different angles. Aeromeccanica [4] presents an unmanned aerial vehicle equipped with an omnidirectional camera with two optics having  $>200$  degree FOV. Additionally, an infrared (IR) camera is also mounted on the drone.

Technest has been awarded by US Navy Small Business Innovative Research program with the project [5] 'Real-Time Omni-Directional Hyperspectral Imager'. The defined system uses compact mega pixel IR and MWIR capable sensors and supposed to capture a 360 degree FOV by using a rotating system that captures 180 degree FOV at a time. Similarly, a rotating spectral imaging system is used to capture large FOV in the studies [6–8]. Hirai *et al.* [6] combines three technologies: HDR, spectral and omnidirectional imaging. They use an automatically rotating mechanism. An RGB camera is supported by filters in order to acquire six band multispectral data between 400 and 700 nm. They perform a correction algorithm on spectral images to reduce the illumination related noises. Karaca *et al.* [8] develops a multiband stereo matching algorithm on a panoramic stereo hyperspectral imaging system. Additionally, they perform a depth estimation on panoramic hyperspectral data set. However, in this study, we propose to develop an omnidirectional hyperspectral system that captures 360 degree FOV in a single image without using a rotating mechanism.

Daniilidis *et al.* [9] has filed a patent regarding a multispectral and omnidirectional imaging system that contains a series of view and reflecting mirrors for splitting the electromagnetic spectrum into two or more bands, and corresponding cameras placed relative to the reflecting mirrors. Although the system is innovative for its time, its multispectral representation capacity is well behind today's technology.

In terms of hyperspectral omnidirectional imaging, there are few previous studies. The closest work to ours, presented in [10], uses  $3 \times 3$  spectral coated catadioptric mirror grid. A plenoptic function records the radiance from the scene from every location, at every angle, for every wavelength and at every time. They perform a sparse representation on depth estimation problem by using the system. However, the spectral density of their proposed system depends on the number of coated mirrors, which is nine. Our work, on the other hand, is entirely hyperspectral and we investigate unmixing approaches in catadioptric domain for the first time.

Omnidirectional images introduce a radial warping due to the structure of the mirror used in the system. As some of the studies [11–14] develop algorithms without modifying the elliptic structure of the scene, others [15–18] prefer to transform the image to the panoramic view, and they work on linear representation. For the applications where the spatial non-uniformity does not affect the performance of the algorithm, we aim to avoid the costly process of generating panoramic view. Thus, we benefit the spectral content of the pixel without need of spatial linearity. Hyperspectral imaging with its high spectral density adds value to remote sensing applications due to its spectral density rather than the provided spatial information.

On the other hand, [19, 20] are examples for large FOV hyperspectral imaging systems with fish-eye lenses. In [19], the spectral analysis of ecological light pollution is performed by using full-spherical fish-eye lens imaging. Similarly, in [20], they perform a visible range hyperspectral monitoring of auroras by using a fish-eye camera.

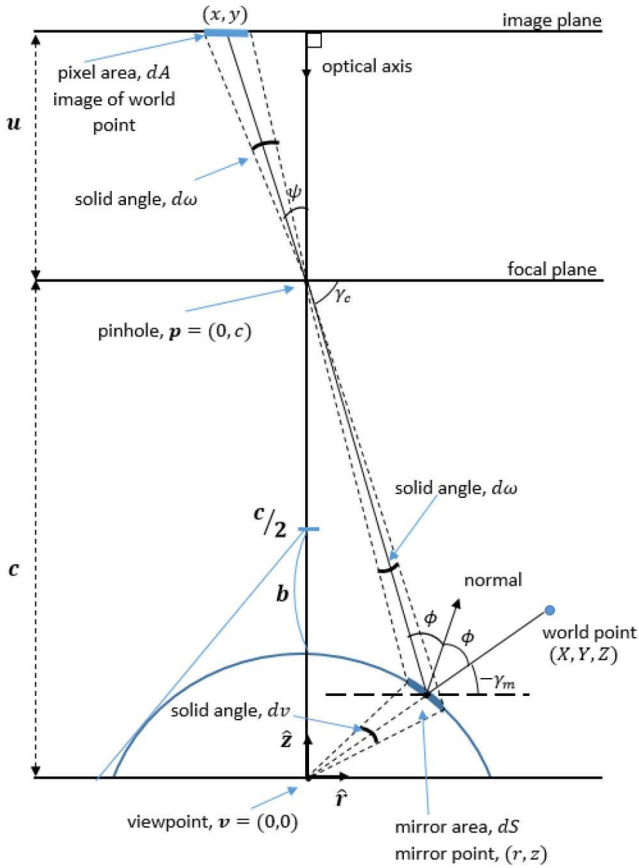


Fig. 2 Image formation in a catadioptric camera with a hyperboloidal mirror

### 3 Background

#### 3.1 Catadioptric image formation

In the proposed system the spatial resolution decreases from periphery of the omnidirectional image to its centre. In this study, we have demonstrated this effect both theoretically and practically. Baker and Nayar [21] presented the single-viewpoint geometry of the catadioptric image formation in their fundamental work. They deeply analyse the different mirror shapes which are used in the catadioptric system. They include a preliminary analysis of the defocus blur caused by the use of a curved mirror. An expression for the spatial resolution factor of a catadioptric sensor is derived in the study. The factor is based on a condition which assumes that while the mirror is positioned in the effective viewpoint  $v$ , the camera must be positioned in the effective pinhole  $p$ . In Fig. 2, the mirror geometry is illustrated in detail based on the studies in [21, 22]. The mirror parameters are  $a$ ,  $b$  and  $c$  where  $c$  is the distance between pinhole and viewpoint in other terms the camera and the mirror, and  $c$  is given by  $c = 2\sqrt{a^2 + b^2}$ . As described in [21], the resolution of the catadioptric sensor is  $dA/dv$  where  $dA$  is the pixel area on the image and  $dv$  is the infinitesimal solid angle viewing the world. The variables used in the following equations are demonstrated in Fig. 2. The resolution of the conventional camera was derived in [21] as

$$\frac{dA}{d\omega} = \frac{u^2}{\cos^3 \psi} \quad (1)$$

Then, the area of the mirror ( $dS$ ) imaged by the infinitesimal area ( $dA$ ) is

$$dS = \frac{d\omega \cdot (c-z)^2}{\cos \phi \cos^2 \psi} = \frac{dA \cdot (c-z)^2 \cdot \cos \psi}{u^2 \cos \phi} \quad (2)$$

The solid angle  $dv$  can be defined as

$$dv = \frac{dS \cdot \cos \phi}{r^2 + z^2} = \frac{dA \cdot (c-z)^2 \cdot \cos \psi}{u^2 (r^2 + z^2)} \quad (3)$$

where  $(r, z)$  is the point on the mirror being imaged. Hence the equation of the resolution of catadioptric sensor can be re-written as

$$\frac{dA}{dv} = \frac{u^2 (r^2 + z^2)}{(c-z)^2 \cdot \cos \psi} = \left[ \frac{(r^2 + z^2) \cos^2 \psi}{(c-z)^2} \right] \frac{dA}{d\omega} \quad (4)$$

But, since

$$\cos^2 \psi = \frac{(c-z)^2}{(c-z)^2 + r^2} \quad (5)$$

we have

$$\frac{dA}{dv} = \left[ \frac{r^2 + z^2}{(c-z)^2 + r^2} \right] \frac{dA}{d\omega} \quad (6)$$

The resolution of the catadioptric camera is the multiplication of the resolution of the conventional camera with the factor  $res$  which is given by

$$res = \frac{r^2 + z^2}{(c-z)^2 + r^2} \quad (7)$$

Note that the factor in (7) is the square of the distance from the point  $(r, z)$  to the effective viewpoint  $v$  divided by the square of the distance from the point  $(r, z)$  to the pinhole  $p$ . Hence the spatial resolution is highest around the periphery.

#### 3.2 Spatial resolution factor

The spatial resolution factor is derived in (7). However, in the implementation phase, the expression needs to be represented in terms of image point coordinates. The relation between mirror parameters, image point coordinates and 3D outgoing ray are explicitly set up by Onoe *et al.* in [22]. The study generates panoramic and perspective images from omnidirectional video streams.

In this subsection, we aim to briefly explain the relation between catadioptric image point coordinates and mirror parameters. As illustrated in Fig. 2, a ray coming from the world point  $P(X, Y, Z)$  toward the focal point  $v$  of the hyperboloidal mirror is reflected by the mirror and passes through the other focal point (camera centre)  $p$ , and the ray intersects an image plane at a point  $p(x, y)$ . This hyperboloidal projection yields the equations in [22] as

$$\gamma_c = \tan^{-1} \frac{u}{\sqrt{x^2 + y^2}} \quad (8)$$

$$\gamma_m = \tan^{-1} \frac{(b^2 + (c/2)^2) \sin \gamma_c - 2b(c/2)}{(b^2 - (c/2)^2) \cos \gamma_c} \quad (9)$$

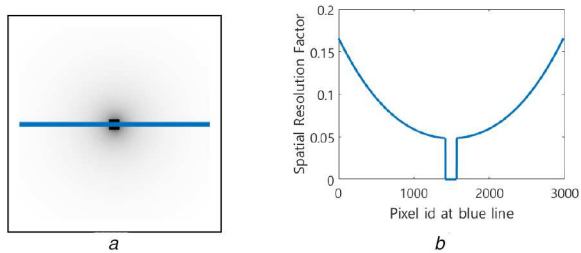
where  $(x, y)$  are the image point, and  $u$  is the focal length of camera lens (the distance between the point  $p$  and the image plane).

On the other hand, Baker and Nayar [21] present the relation between the mirror angle ( $\gamma_m$ ) and the mirror points

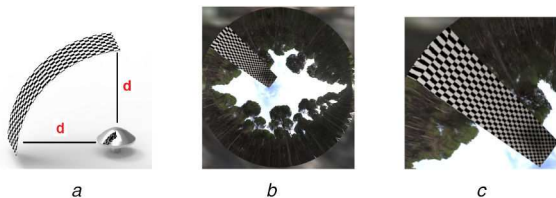
$$\tan(-\gamma_m) = \frac{z}{r} \quad \tan(\gamma_c) = \frac{c-z}{r} \quad (10)$$

By using the equations between (8) and (10),  $r$  and  $z$  can be re-written as

$$r = \frac{c}{\tan(-\gamma_m) + \tan(\gamma_c)} \quad z = \tan(-\gamma_m)r \quad (11)$$



**Fig. 3** Illustrations about the spatial resolution values (a) Spatial resolution map (the values are presented in greyscale), (b) Resolution factors of the pixels at the corresponding line in (a)



**Fig. 4** Illustrations about the simulated image (a) Front view of the simulated scene, (b) Omnidirectional image, (c) Zoom on the checkerboard to better observe the resolution difference

Therefore, we can obtain the parameters  $(r, z)$  in the spatial resolution factor equation (see (7)) by using the image coordinates  $(x, y)$ .

We simulated the image generated according to the coordinate system of an omnidirectional image. The mirror parameters are selected the same with NeoVision hyperbolic mirror ( $a = 28.095, b = 23.4125$ ). Fig. 3a illustrates the change on the resolution of the simulated omnidirectional image in greyscale format where dark colours imply the lower spatial resolution values. This illustration helps us to make an inference about the decrease of the spatial resolution through the mirror centre. The range of the resolution values are plotted in Fig. 3b. The distance  $d$  shown in Fig. 4a is equal for the upper and bottom part of the checkerboard. In this demonstration, while preserving the distance to mirror on each point of the object, we still observe distortion and change on the resolution (Figs. 4b and c). For an image with size of  $(164 \times 164)$ , the resolution factors vary to values between 0.16 and 0.05.

### 3.3 Hyperspectral unmixing

In remote sensing applications, the neighbouring objects can be captured in a single pixel. Hyperspectral imaging makes it possible to discriminate and identify the materials existing in the pixel, and their corresponding mixing ratios. The pure spectral signature of a material is called as endmember. The unmixing approach is an umbrella term that encompasses the estimation of endmember spectra, estimation of the number of endmembers and the estimation of their abundances. The abundance of endmember determines the proportion of the endmember in a pixel. The general definition of a linearly mixed data is

$$x_{ij} = \sum_k e_{ik} c_{kj} + n_{ij} \quad (12)$$

where  $i, j$  and  $k$  correspond to band, pixel and endmember indices, respectively. Additionally,  $x$  is the intensity value,  $e$  is the spectrum,  $c$  is the mixing proportion and  $n$  is the random error. The mixing proportions should sum to one.

Most of the unmixing approaches in the literature assume that the hyperspectral data is spread in a convex structure, and they use this assumption as a base for endmember extraction. However, this assumption requires the number of the pure materials to be known a priori. Therefore, the first step in unmixing algorithms is to estimate the number of endmembers. Hyperspectral signal identification by minimum error (HySime) developed by Bioucas-Dias and Nascimento [23] is one of the well-known algorithms in

the literature for estimating the number of endmembers. We implemented HySime for this purpose in our proposed algorithm. The method is an unsupervised eigen-decomposition based approach. It selects the signal subspace in the least squared error sense.

In spectral unmixing analysis, the following step is the extraction of the endmembers' spectral signatures. In the last step, the abundance fractions are computed. Several least squared error based algorithms are proposed in the literature for this purpose [24–27]. These algorithms vary according to their constraints on abundance values (e.g. non-negativity and sum-to-one constraints). In this study, we use a fast non-negativity constrained least squares algorithm [28], and then we normalised the abundances so that sum-to-one constraint is satisfied.

Bioucas Dias *et al.* [29] present a comprehensive review on hyperspectral unmixing. The study provides to clearly understand the term and techniques of unmixing area. On the other hand, as deep learning has recently attracted much attention in many domains, convolutional neural network architecture is used on pixel-based and cube-based unmixing analysis by Zhang *et al.* [30].

**3.3.1 Geometrical unmixing approaches:** In the literature, geometrical studies are mostly preferred due to their high performance and low computational complexity. Well known algorithms pixel purity index (PPI) [31], N-FINDR [32] and vertex component analysis (VCA) [33] assume the existence of pure pixels for each endmember.

N-FINDR [32] is based on the fact that in spectral dimension the volume defined by a simplex formed by the purest pixels is larger than any other volume defined by any other combination of pixels. Therefore, all pixels are evaluated in the algorithm. This algorithm finds the set of pixels defining the largest volume by inflating a simplex inside the data. The number of iterations is equal to number of pixels times number of endmembers ( $N \times p$ ).

The PPI [31] algorithm projects every spectral vector onto skewers, defined as a large set of random vectors. The points corresponding to extrema, for each skewer direction, are stored. A cumulative account records the number of times each pixel is found to be an extreme. The pixels with the highest scores are the purest ones. The algorithm iterates as the number of skewers ( $num\_skewers$ ).

The VCA [33] algorithm is based on the assumption that the endmembers are the vertices of a simplex. The data is carried in this simplex of minimum volume. The algorithm iteratively projects data onto a direction orthogonal to the subspace spanned by the endmembers already determined. The new endmember signature corresponds to the extreme point of the projection. The algorithm iterates until all endmembers are exhausted ( $p$ ).

The pseudo codes of the algorithms discussed above are given in Appendix section.

**3.3.2 Spatial-contextual unmixing approaches:** Another approach in unmixing literature is the incorporation of spatial information into the spectral unmixing. As it is discussed in [29], the geometrical-, statistical- and sparsity-based approaches work on spectral domain, and ignore the valuable information in spatial domain. Researchers are motivated to classify hyperspectral images by exploiting the correlation between both spatial and spectral neighbours. The idea in this approach is to utilise the spatial information in addition to the spectral unmixing algorithms at the expense of additional computational cost.

In the proposed catadioptric hyperspectral imaging system, we aim to utilise the difference in spatial resolution between the centre and outer parts of the mirror and furthermore to account for the distortion in the mirror. As the spatial resolution decreases toward the image centre, the possibility of detecting pure pixels in the regions toward the image periphery increases. Therefore, the spatial-spectral unmixing approaches are employed in this section. Xu *et al.* [34] and Yan *et al.* [35] fuse spatial and spectral information in a sub-pixel level. Region-based spatial preprocessing (RBSPP) [36], spatial preprocessing (SPP) for endmember extraction [37] and automated morphological endmember extraction (AMEE) [38] are well known spatial-

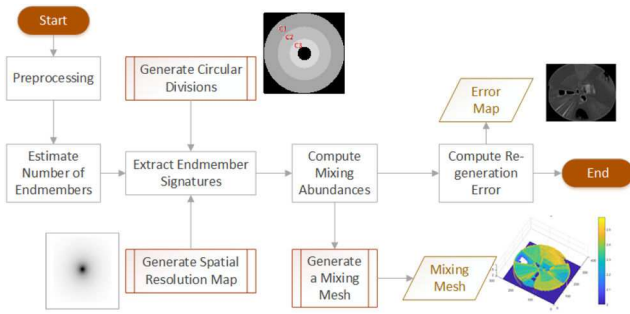


Fig. 5 General flowchart of the proposed algorithm

contextual unmixing algorithms. The studies [34, 35] perform a sub-pixel spectral mixture analysis. AMEE and SPP are pixel-based unmixing approaches, and RBSPP and SSPP are region-based approaches. In the proposed system, the endmembers are extracted from the individual regions which are partitioned according to their spatial resolutions. Therefore, region-based unmixing approaches are more related with the proposed study. Martin and Plaza [39] proposed an improved version of RBSSP in SSPP. Hence, the proposed algorithm is only compared with RBSPP and SSPP based on the experimental results presented in their study.

RBSPP [36] uses spatial information as a guide to exploit spectral information more effectively by adequately exploiting spatial context in adaptive fashion. This approach first adaptively searches for the most spectrally pure regions. Then the method performs unsupervised clustering using the ISODATA [40] algorithm, and finally applies the orthogonal subspace projection algorithm to the mean spectra of the resulting regions in order to find a set of spatially representative regions with associated spectra which are both spectrally pure and orthogonal between them.

SSPP [39] considers spatial and spectral information simultaneously and fuses both sources of information at the preprocessing level. First, a spatial homogeneity index is computed by using the difference between the original and spatially filtered image. Second, a principal components transformation is performed. A spectral purity index is defined according to the distances of the pixels to the maxima and minima of the projection. SSPP algorithm depends on two thresholds. Threshold  $\rho \in [0, 100]$  controls the pixels selected based on spatial homogeneity. Threshold  $\beta \in [0, 100]$  controls the pixels selected based on spectral purity. In parallel to the first two steps, an unsupervised spectral clustering algorithm (ISODATA [40]) is performed. The rest of the algorithm is region-based. The regions with high spectral purity and high spatial homogeneity are selected. The endmember selection process is only performed on these selected regions. Therefore, the processing time of the endmember estimation process significantly decreases.

## 4 Methodology

Spectral signature mixing is a commonly faced problem caused by low spatial resolution in hyperspectral imagery. It becomes a more challenging problem in omnidirectional images. Objects are represented with fewer numbers of pixels towards the mirror centre due to the mirror shape. This reduction in the spatial resolution causes mixed pixels to be located around the mirror centre. In this study, we propose the application of approaches which take into consideration the locations of the pixels on the mirror. A general flowchart of the algorithm is given in Fig. 5. The algorithm starts with estimating the pure pixels and their abundance values. Since distinguishing the unique materials in a scene is nontrivial, obtaining a groundtruth for the endmember estimation is problematic. Instead, the data is reversely generated by using the estimated pure pixels and abundances. The difference between the original and the regenerated data indicates the validity of the proposed algorithm. The validity of all unmixing steps are examined together.

### 4.1 Proposed improvement on geometrical unmixing approach (omni-approach)

The method that we propose is similar to the conventional spatial-spectral preprocessing unmixing approaches. However, unlike these methods, it does not require spatial connectivity. It aims to overcome the inequality of spatial resolution that occurs in the omnidirectional hyperspectral image. Since the spatial resolution factor is directly related with the mixing of the scene, we rate the pixels according to their spatial resolution factors. In the proposed preprocessing step, the spatial resolution map is generated by using the camera and mirror parameters (explained in Section 3.2). In this respect, the preprocessing step proposed in this study is independent from the scene content. Then, the map is integrated with the endmember estimation algorithm to be applied. The complexity of the proposed approach is  $O(n)$  where  $n$  is row  $\times$  column of the omnidirectional image. Therefore, the effect on the endmember estimation algorithm is negligible in terms of processing time. This provides a great advantage compared to the other spatial-spectral unmixing methods.

The methods that are evaluated in this study are geometry based approaches and they aim to extract the endmember signatures by maximising the volume. Under the assumption that the endmembers must be located at the extrema, we propose to multiply the data by the spatial resolution map just before detecting the maxima of the volume. Thus, the point having high spatial resolution is translated to outer of the simplex. The possibility of detecting a point having higher spatial resolution as an extreme point is increased in this way. Conversely, the pixel with lower resolution is forced to translate to inner position in the data cloud. The maxima of the algorithms are evaluated in the Line #6 of PPI, Line #10 in N-FINDR (Appendix section), and Line #19 in VCA [33].

### 4.2 Proposed local endmember extraction approach on omnidirectional images

The materials present in the scene may have diversity on their spectral characteristics, even though they are pure pixels conceptually. Different environmental and illumination conditions such as shadow of an object and heterogeneous content of the material cause a variety on the pure spectral signatures of the material. A single representer for each class for the complex unmixing problem may not be found. For these reasons, some researchers prefer to conduct their unmixing studies on local endmember estimation approach [41, 42]. This approach investigates the spectral unmixing algorithms in a small size window independently from the rest of the scene. Somers *et al.* [41] introduced a similar algorithm. They select subsets from the hyperspectral data cube. The extracted endmembers from the subsets are stored in a global endmembers set, and then clustered in order to obtain the global representers of the pure materials. This algorithm is also used in [42], which aims to monitor seasonal variations of vegetation cover. They estimate the abundances of the endmembers with a different viewpoint. The data cube is evaluated using the global endmembers set, then the abundances of the endmembers belonging to the same cluster are accumulated for each pixel. As a conclusion, they indicate that the local unmixing idea benefits to discriminate two similar vegetation species.

In our study, we propose that spectral analysis of partitioned circles which are generated according to their spatial resolution factors, is more appropriate for omnidirectional hyperspectral images. The materials with different spatial resolutions may have a diversity on their spectral signatures. Local unmixing approach prevents to miss these cases. The scheme of the proposed algorithm is depicted in Fig. 6. The image is divided into three circles with equal number of pixels. The estimation of the number of endmembers and estimation of spectral signatures of endmembers (EEA) are studied independently on each circle. The first column depicts the estimated pure pixel locations with red dots on the image, their corresponding spectra are plotted in the following column. After endmember estimation, a bundle of endmembers is accumulated. The studies presented in [41, 42] take advantage of high number of endmembers by using multiple endmember

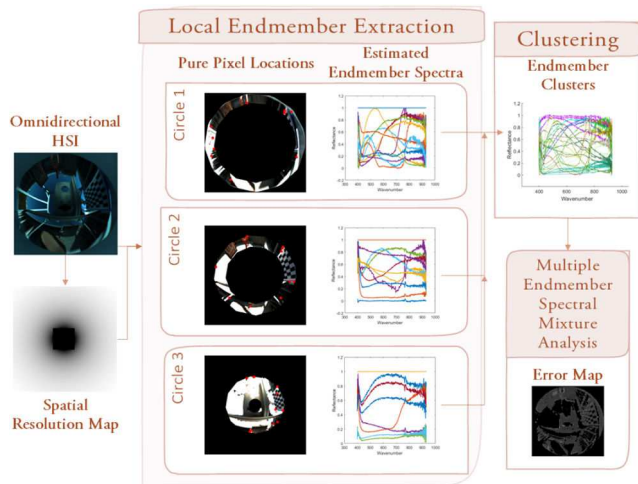


Fig. 6 Scheme of the proposed local endmember extraction algorithm

spectral mixture analysis (MESMA) [43]. The algorithm is based on using a library which contains field and laboratory measurements. An enhanced performance of MESMA is presented at [44]. A wide range of instances according to the application is collected. In spectral mixture analysis, it achieves to discriminate similar spectra [43]. In the proposed algorithm, we do not use such a library. Instead, we use the internal information of the hyperspectral data as it is proposed in [41]. A library is created by collecting the results of endmember estimation of each circular sub-region. The collected endmembers set is clustered by  $k$ -means [45], and an optimal abundance map is computed by using MESMA. The last column consists of the clustered endmembers and the error maps where white colour indicates higher error. The definition of error map is presented in Section 5.3. Note that, the proposed method is combined with the improvement explained in Section 4.1. The pixels in the circular sub-regions are multiplied with their corresponding spatial resolution factor.

As a conclusion of this section, the first method is proposed for geometrical unmixing approaches. Most of the geometrical approaches in the literature assume that the hyperspectral data is spread in a convex structure. As each pixel in a catadioptric image has different spatial resolution factor, the mixing ratio of the pixels depend on their spatial resolution. The pixel with higher spatial resolution is more likely to contain a pure spectral signature, in other words less mixed signature. We propose to rate the pixels in the convex structure according to their spatial resolution factors. The second method proposed in this study is a local spectral mixing analysis approach. The local unmixing algorithms spatially divide the hyperspectral scene rather than inspecting the whole scene at once. This point of view in unmixing problem produces more robust and accurate results.

## 5 Experimental results

In this section, the well-known geometrical unmixing approaches and the proposed improvements on geometrical and spatial-contextual unmixing approaches are evaluated. The validity of pure pixels extracted by the proposed method are ensured by regenerating data. The abundance map of the data is computed by the extracted pure pixels. The data is regenerated by multiplying the estimated pure pixels and the abundance map (see (12)). The difference between regenerated and original data indicates the regeneration error (see (13)). The accuracies of the algorithms are compared to each other using regeneration error.

### 5.1 Data definition

The proposed study is a pioneer on integrating hyperspectral imaging devices and catadioptric mirrors. According to our limited knowledge, there is not any public data set to evaluate the proposed method. Therefore, we have performed some acquisitions. In the experiments, 17 images are evaluated. While the first 11 of them

are real world acquisitions, the last six images are synthetically generated catadioptric hyperspectral images.

**5.1.1 Real world acquisitions:** The proposed method is tested on scenes that have been acquired by Headwall A-Series Visible + NIR linescan camera with spectral range of 400 – 1100 and 1.5 nm spectral resolution. The spectral range of the catadioptric system is the same with the range of the camera which views the mirror. Additionally, we used the hyperbolic mirror of NeoVision. We performed outdoor acquisitions in all experiments of our study. We have acquired three real world data sets which contain totally 11 images. The images in a data set include same objects in a variety of positions and illumination conditions. All datasets contain building, sky and forest in some scenes. Additionally, white reflector (teflon) and black reflector is used for reflectance conversion.

- **Data set #1:** In the first acquisition, several objects made of clay and mosaic are captured in addition to the materials discussed above. Experiments #1 and #2 belong to Data set #1.
- **Data set #2:** The scene is composed of the materials with distinctive spectral characteristics in VNIR region. Bone, vegetation and soil residues can exist together in archaeological remote sensing and food inspection problems. Experiments #3, #4 and #7 to #11 belong to Data set #2.
- **Data set #3:** The scene contains printed papers with six different colours on different geometrical shapes. The shapes are painted by using red, green, blue, magenta, cyan and yellow colours. The first print covers six colour stripes which lie from outer regions to the centre of the image. Two of the prints are painted by red, green and blue, and the squares' size are  $1\text{ cm}^2$  and  $2\text{ cm}^2$ . The last paper is designed contrary to the premise of the proposed algorithm. The proposed study is divided into three parts from outer to the centre of the image. Each part contains different two coloured squares. The colours which exist in the inner part, do not exist in the outer part. Experiments #5 and #6 belong to Data set #3.

The sample RGB representations of the data sets and the materials that exist in the scene are given in Fig. 7.

**5.1.2 Synthetic data:** We have simulated a four-wall indoor scene. Each wall is composed of a signature gathered from the Indian Pines data set [46]. The generation of synthetic data is similar to that in [47]. The walls have a pattern of squares with two pixel width where the consecutive squares have different spectral characteristics. Totally 11 different spectral signatures are used in a simulated image. Fig. 8a demonstrates the RGB representation of the synthetic data. After assigning the pure spectral signatures to the regions, an averaging low-pass filter is applied in order to spectrally mix the data. Fig. 8b is the mixing map of the scene, the map demonstrates the mixing ratios of each pixel. The highly mixed pixels get higher values in the map. The ratio is computed by multiplying the abundances of a pixel. The synthetic data is categorised into four parts:

- No noise, pure spectral signature (Experiment #12)
- Noisy, pure spectral signature (Experiments #13 and #14)
- Noisy, spectrally mixed (Experiments #15 and #16)
- No noise, spectrally mixed (Experiment #17)

### 5.2 Limitations

The hyperspectral sensor requires a stable light source in order to obtain an accurate measurement for indoor acquisitions. For omnidirectional imaging, multiple illuminators must be integrated for the diffuse illumination of the environment to be captured. We performed only outdoor acquisitions because of the insufficient illumination equipment.

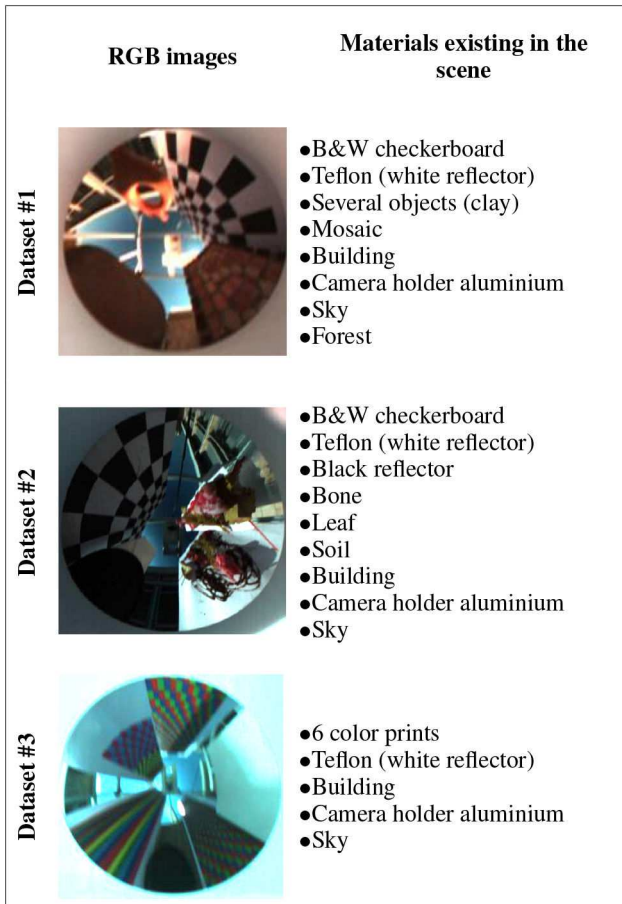


Fig. 7 Details of the real world acquisitions

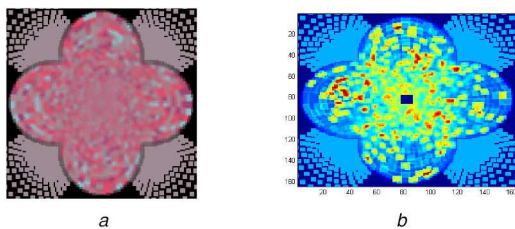


Fig. 8 Visualisations of the spectral mixing proportions  
(a) Synthetic omnidirectional hyperspectral data, (b) A sample mixing map

### 5.3 Comparison of unmixing algorithms and preprocessing approaches

In this subsection, we compare the effect of the spatial-contextual preprocessing approaches on the geometrical unmixing algorithms in terms of regeneration error. The methods are compared on the error of regenerated data which is created by using the extracted end members. The error values are multiplied by 100 for display purposes. The regeneration error is computed by root mean squared error as in

$$\text{error} = \sqrt{\frac{\sum_{i=1}^N (\mathcal{S}(i, :)^2 - \mathbf{X}(i, :)^2)}{N}} \quad (13)$$

where  $\mathcal{S}$  is original hyperspectral data,  $\mathbf{X}$  is measured hyperspectral data and  $N$  is total number of pixels.

In Table 1, the first super-column (containing three columns) shows the results of the geometrical unmixing algorithms without any spatial-spectral preprocessing. The following three super-columns contain the results of the spatial-spectral preprocessing approaches (RBSPP, SSPP and omni-approach) applied before the regarding geometrical unmixing approaches. The experiments whose results are shared in Table 1, the data ID between 1 and 11 are the real world acquisitions, and the rest correspond to the

simulated omnidirectional hyperspectral data. The signal to noise ratio (SNR) of the data are given in Table 2. The last row of Table 1 indicates the overall accumulated error values of the experiments. These overall results provide us to make a comprehensive comparison of the geometrical and spatial-contextual unmixing approaches. The proposed method is also compared with two other spatial-contextual methods: AMEE and SPP. However they were not included in Table 1, since their regeneration errors are higher than that of RBSPP and SSPP. The lowest overall error is obtained when N-FINDR algorithm is applied with omni-approach. Additionally, omni-approach achieves to decrease the overall error of VCA. SSPP algorithm depends on two thresholds:  $\rho$  and  $\beta$ . The results of SSPP demonstrated in Table 1 are obtained by using the default  $\rho$  and  $\beta$  values provided in Matlab implementation, where  $\rho = 50$ ,  $\beta = 30$ . The effect of the thresholds on SSPP approach is investigated in Fig. 9. All combinations of the  $\rho$  and  $\beta$  parameters for the values 30, 50 and 70 are evaluated as it is suggested in the related study [39]. The lowest error of SSPP + NFINDR is obtained when  $\rho = 50$ ,  $\beta = 70$ . The lowest error of SSPP + PPI is obtained when  $\rho = 70$ ,  $\beta = 70$ . The lowest error of SSPP + VCA is obtained when  $\rho = 70$ ,  $\beta = 50$ . On the other hand, the endmember estimation accuracy of SSPP approach highly depends on the estimated number of endmembers. The SNR modification discussed in Section 3.3 negatively affects the spatial segmentation step. SSPP uses the output of an external method: ISODATA method of ENVI software. The performance of SSPP approach also depends on the clustering performance of ISODATA. In this case, SSPP remains incapable of decreasing the regeneration error of the geometrical unmixing algorithms.

### 5.4 Evaluation of the proposed improvement on geometrical approaches

In this subsection, we aim to observe the effect of the proposed improvement explained in Section 4.1 on the existing geometrical unmixing algorithms. Figs. 10 and 11 represent the case which satisfies the situation that the proposed improvement is based on. The first column in the table shows the RGB representations of the scenes. The upper row contains the error maps created by VCA and OmniVCA algorithms. Bright tones indicate higher error, dark tones indicate lower error. The second row shows the estimated pure pixel locations on the RGB images of the data. The last row indicates the regeneration errors of the N-FINDR, PPI and VCA algorithms with and without omnidirectional approach.

### 5.5 Evaluation of the proposed local endmember extraction approach

In this subsection, we evaluate the endmember estimation performance of the algorithm proposed in Section 4.2. Fig. 12 demonstrates the comparison of the number of endmembers estimated from individual circles versus whole image. Circle 1 is the outer, and the circle 3 is the inner one. In the experiments between #12 and #17, 11 different spectral signatures are used. The number of endmembers are estimated highly correlated with the groundtruth in the Exp. #12, #13 and #17. In the Exp. #14, #15 and #16, the noise is increased, and the data is manually mixed. Consequently, estimation accuracy is decreased in these experiments. In most of the experiments, the estimated number of endmembers are similar to each other between circles. However, in Exp. #3, #4 and #5, the estimated number of endmembers are explicitly increased in inner circles. The extracted endmember locations are demonstrated in Figs. 13–15. As it can be analysed in the RGB representations, there is no significant material diversity difference between inner and outer circles. The reliability of Hysime is highly dependent on SNR estimation accuracy. In the provided Matlab code by the authors, the SNR is assigned a value of 50 as default. However, it fails in some cases and the algorithm grossly over-estimates the number of endmembers as in Fig. 16. The high number of estimated endmembers provides regenerating the data with lower error. In other respects, the difference between the numbers of endmembers of circles is not reasonable. Therefore, we modified the implementation of the SNR prediction as

**Table 1** Regeneration error based comparison of geometrical unmixing algorithms with and without preprocessing approaches (OE: overall error)

Exp.#	Geometrical approaches						Spatial-spectral approaches					
	No preprocessing			RBSPP			SSPP			Omni-approach		
	NFINDR	PPI	VCA	NFINDR	PPI	VCA	NFINDR	PPI	VCA	NFINDR	PPI	VCA
1	1.97	3.85	1.81	9.16	2.75	2.70	1.94	4.40	2.40	1.72	5.74	1.86
2	2.26	7.27	2.92	1.79	37.9	1.72	2.43	7.01	4.94	2.12	8.12	2.92
3	1.35	4.76	2.49	2.89	26.3	1.33	1.46	2.67	2.00	2.13	2.39	1.75
4	1.05	2.57	1.04	1.03	1.61	1.06	1.05	2.16	0.94	1.05	2.87	0.97
5	2.68	9.43	2.71	5.90	27.3	5.94	5.19	19.35	3.14	2.51	12.38	2.78
6	2.47	9.33	2.42	2.73	6.21	2.69	11.90	10.23	2.51	2.56	9.43	2.63
7	3.85	5.21	1.62	1.50	6.22	1.51	5.13	4.46	1.91	1.90	5.21	1.76
8	1.52	4.19	1.46	3.08	20.2	2.97	1.49	4.15	1.43	1.50	3.92	1.61
9	1.71	3.54	1.60	3.01	19.5	3.01	1.60	4.00	1.46	1.43	3.76	1.55
10	1.36	3.25	1.57	1.25	1.23	1.15	1.37	2.35	1.33	1.42	2.41	1.57
11	1.50	6.84	2.69	2.06	49.1	1.84	1.57	6.06	2.38	1.39	6.37	2.69
12	0.03	21.76	0.00	3.99	33.53	3.99	0.03	23.31	0.00	0.03	21.76	0.00
13	0.09	8.17	1.67	1.14	25.08	1.16	0.10	8.52	0.70	0.07	7.21	1.69
14	0.87	9.53	0.57	2.20	1.99	2.13	0.86	10.12	0.57	0.68	9.08	0.57
15	0.15	7.77	1.69	3.36	29.93	3.36	0.15	7.86	1.19	0.14	7.02	1.68
16	0.99	8.89	0.68	3.51	31.25	3.50	1.00	10.44	0.68	0.80	9.05	0.68
17	0.09	18.87	0.08	3.68	32.76	3.68	0.12	25.82	0.11	0.09	18.87	0.07
OE	23.94	135.22	27.02	52.27	352.87	43.74	37.39	152.88	27.70	21.53	135.58	26.78

**Table 2** SNR values and the data sets belonging to the experiments (low SNR value indicates high noise, SIM: simulated data)

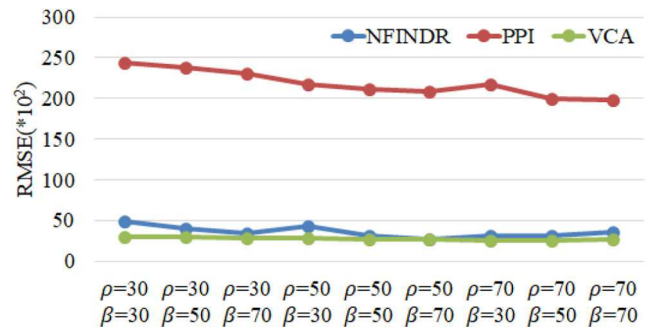
Exp.#	1	2	3	4	5	6	7	8	9	10	11	12	13	14	15	16	17
data set#	1	1	2	2	3	3	2	2	2	2	2	sim.	sim.	sim.	sim.	sim.	sim.
SNR	31	30	34	26	29	26	28	32	32	26	34	no noise	50	30	50	30	no noise

$$SNR \equiv 10 \log_{10} \frac{x^2}{s^2} \equiv 10 \log_{10} \frac{[Es^T s]}{[En^T n]} \quad (14)$$

where  $s$  and  $n$  are vectors standing for signal and additive noise, respectively.

As a reminder, the errors are measured per pixel. In other words, the total error of the data is normalised by the total number of pixels. Therefore, the error is independent of the circle size. The proposed improvements are compared in Table 3. The first column shows the regeneration error without using a spatial information. The following column contains the results which obtained by using only the OmniVCA approach. Fig. 17 and Table 3 show that the simulated images produce lower errors due to their comparatively higher SNR values. The last column presents the results of the algorithm where the OmniVCA and local EEA algorithms are used together. The significant contribution is obtained in the local EEA and multiple endmember selection approach. The overall error in this column decreases by 45% compared to the VCA approach with no spatial information.

The experimental results shared in Table 3 correspond to the results of the evaluation of three circles. The performance of the local EEA approach is evaluated for two, three, nine and 18 circular divisions and sub-regions. Therefore, we measure the relation between the subset size and performance of the algorithm. The schemes of the divisions are demonstrated in Fig. 18. The chart in Fig. 17 compares the subset sizes on reconstruction error. The authors of [41] proposed to set the subset size as 10% of the image size. However, in this study, we obtain lowest error by using three circles, in other words, 33% of the image size. The image is partitioned into tori having equal number of pixels. In this case, the inner circle has largest radius, and the outer circle has smallest radius. In most of the scenes, the inner circles capture the highly saturated area, e.g. sky and aluminum camera holder. HySime mostly fails in estimation of number of endmembers in these scenes. Therefore, we continue the studies by keeping equal the number of pixels rather than minor radii. As the region size decreases, the algorithm for estimation of number of endmembers (HySime) underperforms. The output of the HySime algorithm



**Fig. 9** Effect of SSPP thresholds on regeneration error

directly effects the extracted endmember spectra and the regeneration performance.

In this section, the relation between scene content and position of the divider line is also investigated for the vertical divisions. In this experiment, the schema with nine sub-regions is investigated. In each scheme type, the vertical divider line is rotated 60 degrees clockwise five times. Fig. 19 presents the reconstruction error plot for the demonstrated rotation schemes. The errors of most of the experiments are similar for different vertical division except Exp. #2 and Exp. #11. There is a considerable difference between VD2 and VD3 of Exp. #2, and VD3 and VD5 of Exp. #11. Therefore, the error maps of these experiments are examined in Figs. 20 and 21. The rotation of the divider line changes the content of sub-regions. Therefore, the estimated SNR, number of materials and spectral signatures exist in the sub-region are effected by the rotation. Furthermore, these factors affect all steps of the linear unmixing, and consequently, the reconstruction error is changed. This investigation shows that the location of the divider in vertical division may be crucial for some scenes.

To conclude this section, the proposed improvement on geometrical unmixing approaches (omni-approach) specific to the omnidirectional hyperspectral imaging system, succeeded in increasing the estimation accuracy of the state-of-the-art VCA method on most of the experiments. However, scenes which



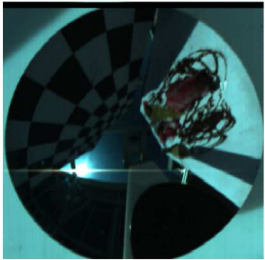
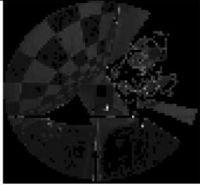
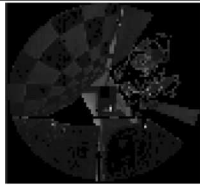


RGB Representation	Error Map of VCA	Error Map of OmniVCA				
						
	Pure Pixel Locations of VCA	Pure Pixel Locations of OmniVCA				
						
	Error of Original Algorithms		Error of Omni Approach			
	NFINDR	PPI	VCA	NFINDR	PPI	VCA
	1.35	4.76	2.49	2.13	2.39	1.75

Fig. 10 Evaluation of the proposed geometrical unmixing improvement on Exp. #3


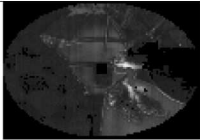
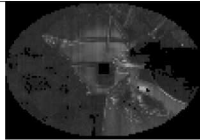


RGB Representation	Error Map of VCA	Error Map of OmniVCA				
						
	Pure Pixel Locations of VCA	Pure Pixel Locations of OmniVCA				
						
	Error of Original Algorithms		Error of Omni Approach			
	NFINDR	PPI	VCA	NFINDR	PPI	VCA
	1.50	2.25	1.44	1.46	2.19	1.30

Fig. 11 Evaluation of the proposed geometrical unmixing improvement on Exp. #4

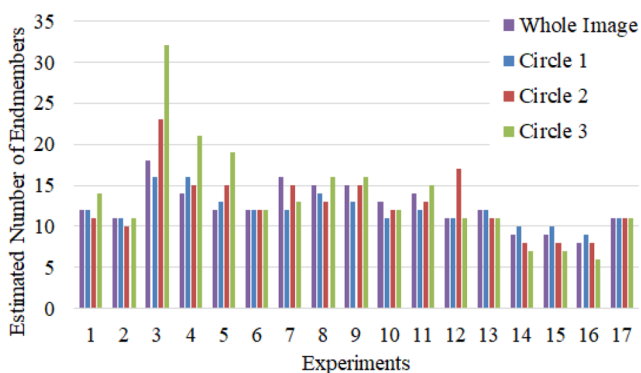


Fig. 12 Estimated number of endmembers on each circular division

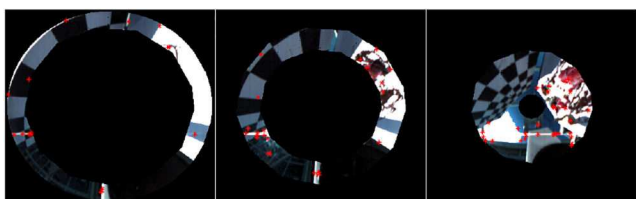


Fig. 13 Extracted endmembers on each circle of Exp. #3

contain different materials on the inner and the outer parts of the mirror limit the potential of the method.

The proposed local EEA method is also developed according to the structure of the omnidirectional hyperspectral imaging system. These two improvements are applied concurrently on hyperspectral data. We conclude that the spectral analysis of omnidirectional data achieves fewer errors on spatially divided parts rather than implementing on whole image. The endmembers and their abundances are properly estimated by using circular divisions.

## 6 Conclusion

The hyperspectral cameras used in remote sensing applications often need large FOV. Recent applications capture large FOV hyperspectral data by using airborne, satellite and UAV systems. In this study, we aimed to increase the FOV of traditional hyperspectral imaging systems. The limitations of existing systems, weather conditions, flight permissions, no fly zones, costly aircraft hire, and carrying capacity of UAVs, are alleviated in low cost and easy-to-use manner. We proposed using line scan cameras on catadioptric systems. To our knowledge, this is the first time that a single hyperspectral camera and a single catadioptric mirror is used together to capture an omnidirectional hyperspectral image.

We analysed the proposed system in the context of spectral unmixing which is one of the most challenging problems of hyperspectral imaging. We identified the critical issues on spectral

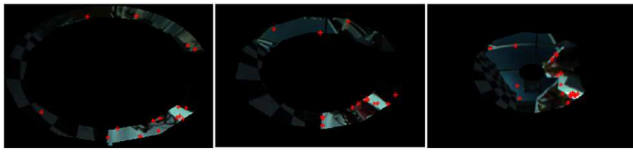


Fig. 14 Extracted endmembers on each circle of Exp. #4

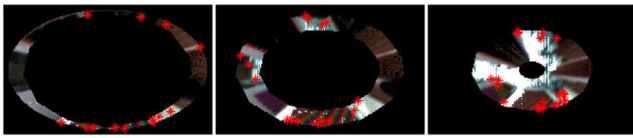


Fig. 15 Extracted endmembers on each circle of Exp. #5

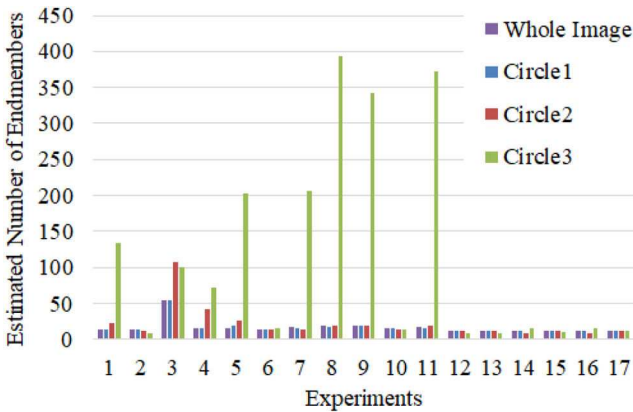


Fig. 16 Over-estimated number of endmembers

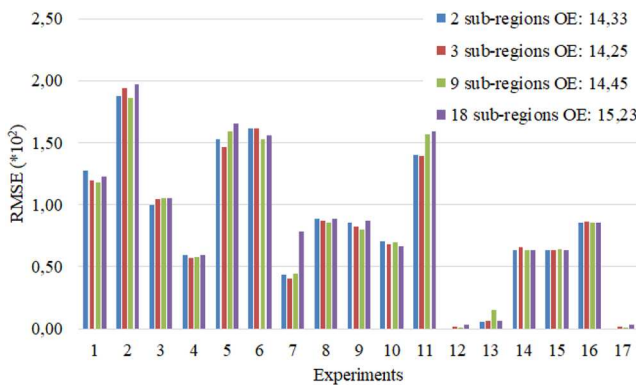


Fig. 17 Reconstruction errors of the division schema given in Fig. 18

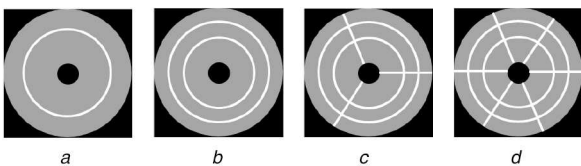


Fig. 18 Division Schema

(a) 2 sub-regions, (b) 3 sub-regions, (c) 9 sub-regions, (d) 18 sub-regions

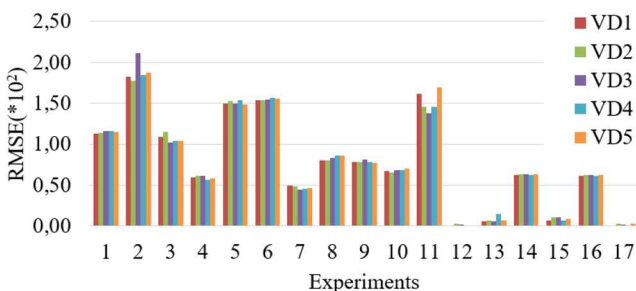


Fig. 19 Reconstruction errors for each vertical division (VD)

Table 3 Regeneration error based performance evaluation of the proposed improvements (OE: overall error)

Exp.#	VCA no preprocessing	VCA omni-approach	VCA omni-approach & local EEA
1	1.81	1.86	1.20
2	2.92	2.92	1.94
3	2.49	1.75	1.05
4	1.04	0.97	0.57
5	2.71	2.78	1.47
6	2.42	2.63	1.62
7	1.62	1.76	0.41
8	1.46	1.61	0.87
9	1.60	1.55	0.82
10	1.57	1.57	0.68
11	2.69	2.69	1.39
12	0.00	0.00	0.00
13	1.67	1.69	0.09
14	0.57	0.57	0.56
15	1.69	1.68	0.49
16	0.68	0.68	0.69
17	0.08	0.07	0.00
OE	27.02	26.78	14.00

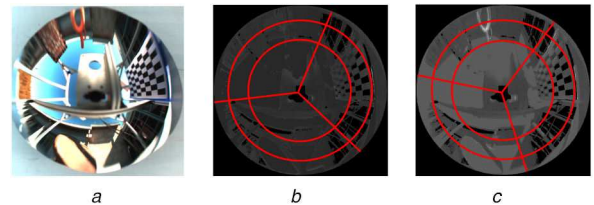


Fig. 20 Effect on RMSE of the vertical division's angular position on Exp. #2

(a) RGB representation of Exp. #2, (b) Error map of VD2. RMSE: 1.78, (c) Error map of VD3. RMSE: 2.11

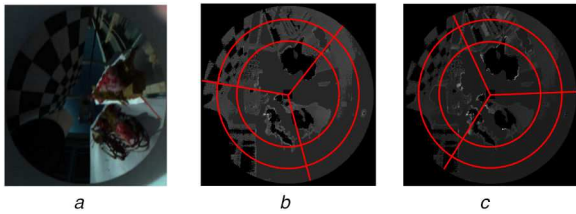
unmixing that must be taken into consideration specifically for the proposed system.

As the region closer to the centre of the mirror has lower spatial resolution, we introduced a weighting scheme to favour pure pixels in the outer part of the mirror. Additionally, the local unmixing approach related to hyperspectral image analysis was adapted specifically to the proposed imaging system, and we developed a new spatially local unmixing approach. The novel approach decreases the regeneration error of the conventional geometrical and spatial-contextual unmixing algorithms on estimating the endmembers and their abundances.

As future work, we suggest an intelligent endmember selection process in the MESMA, e.g. incorporating spectral similarity of the spatially neighbouring pixels, developing an effective clustering method by using the variances. Additionally, regional division step of local unmixing approach can be performed adaptively based on uniform spectral properties of regions instead of equal sized ones. Furthermore, non-linear unmixing analysis can be investigated for catadioptric image formation.

The proposed system covers many application areas belonging to the omnidirectional and hyperspectral imaging. The study may produce a practical solution for the problems which requires wide FOV including gas emission detection, road traffic monitoring, biomedical imaging and surveillance.

The reader is kindly redirected to [33] for the pseudo code of VCA approach.



**Fig. 21** Effect on RMSE of the vertical division's angular position on Exp. #11

(a) RGB representation of Exp. #11, (b) Error map of VD3. RMSE: 1.38, (c) Error map of VD5. RMSE: 1.69

## 7 References

[1] Thomas, C., Ranchin, T., Wald, L., *et al.*: 'Synthesis of multispectral images to high spatial resolution: a critical review of fusion methods based on remote sensing physics', *IEEE Trans. Geosci. Remote Sens.*, 2008, **46**, (5), pp. 1301–1312

[2] Gluckman, J., Nayar, S.K.: 'Catadioptric stereo using planar mirrors', 2001. 1. Available at [http://www1.cs.columbia.edu/CAVE/publications/pdfs/Gluckman\\_IJCV01.pdf](http://www1.cs.columbia.edu/CAVE/publications/pdfs/Gluckman_IJCV01.pdf)

[3] Bastanlar, Y.: 'Structure-from-motion for systems with perspective and omnidirectional cameras'. PhD. Thesis, Middle East Technical University, 2009

[4] Aeromeccanica: 'Fly360'. Available at <http://www.aeromeccanica.it/>

[5] Technest Holdings: 'REAL-time omni-directional hyperspectral imager | SBIR.gov', 2006. Available at <https://www.sbir.gov/sbirsearch/detail/174028>

[6] Hirai, K., Osawa, N., Hori, M., *et al.*: 'High-dynamic-range spectral imaging system for omnidirectional scene capture', *J. Imaging*, 2018, **4**, (4), p. 53. Available at <http://www.mdpi.com/2313-433X/4/4/53>

[7] Tominaga, S., Fukuda, T., Kimachi, A.: 'A high-resolution imaging system for omnidirectional illuminant estimation', *J. Imaging Sci. Technol.*, 2008, **52**, (4), p. 040907. Available at <http://www.ingentaconnect.com/content/ist/jist/2008/00000052/00000004/art00010>

[8] Karaca, A.C., Erturk, A., Gullu, M.K., *et al.*: 'Ground-based panoramic stereo hyperspectral imaging system with multiband stereo matching', *IEEE J.Sel. Topi. Appl. Earth Obs. Remote Sens.*, 2016, **9**, (9), pp. 3926–3940. Available at <http://ieeexplore.ieee.org/document/7302539/>

[9] Danilidis, K., Angelopoulou, E., Kumar, V.: 'Multispectral omnidirectional optical sensor and methods therefor'. Google Patents, 2006. Available at <https://patents.google.com/patent/US6982743>

[10] Xue, Y., Zhu, K., Fu, Q., *et al.*: 'Catadioptric HyperSpectral light field imaging'. 2017 IEEE Int. Conf. on Computer Vision (ICCV), Venice, Italy, 2017, pp. 985–993. Available at <http://ieeexplore.ieee.org/document/8237374/>

[11] Bazin, J.C., Demonceaux, C., Vasseur, P., *et al.*: 'Motion estimation by decoupling rotation and translation in catadioptric vision', *Comput. Vis. Image Underst.*, 2010, **114**, (2), pp. 254–273

[12] Ozisik, N.D., Lopez-Nicolas, G., Guerrero, J.J.: 'Scene structure recovery from a single omnidirectional image'. 2011 IEEE Int. Conf. on Computer Vision Workshops (ICCV Workshops), Barcelona, Spain, 2011, pp. 359–366

[13] Lourenco, M., Barreto, J.P., Vasconcelos, F.: 'sRD-SIFT: keypoint detection and matching in images with radial distortion', *IEEE Trans. Robot.*, 2012, **28**, (3), pp. 752–760. Available at <http://ieeexplore.ieee.org/document/6151178/>

[14] Cinaroglu, I., Bastanlar, Y.: 'A direct approach for object detection with catadioptric omnidirectional cameras', *Signal. Image. Video. Process.*, 2016, **10**, (2), pp. 413–420. Available at <http://link.springer.com/10.1007/s11760-015-0768-2>

[15] Iraqui, A., Dupuis, Y., Boutteau, R., *et al.*: 'Fusion of omnidirectional and PTZ cameras for face detection and tracking'. 2010 Int. Conf. on Emerging Security Technologies, Canterbury, UK., 2010, pp. 18–23. Available at <http://ieeexplore.ieee.org/document/5600047/>

[16] Kang, S., Roh, A., Nam, B., *et al.*: 'People detection method using graphics processing units for a mobile robot with an omnidirectional camera', *Opt. Eng.*, 2011, **50**, (12), p. 127204. Available at <http://opticalengineering.spiedigitallibrary.org/article.aspx?doi=10.1117/1.3660573>

[17] Kawanishi, T., Yamazawa, K., Iwasa, H., *et al.*: 'Generation of high-resolution stereo panoramic images by omnidirectional imaging sensor using hexagonal pyramidal mirrors'. Proc. Fourteenth Int. Conf. on Pattern Recognition, Brisbane, Queensland, Australia, 1998, vol. 1, pp. 485–489

[18] Yamazawa, K., Yagi, Y., Yachida, M.: 'Obstacle detection with omnidirectional image sensor hyperomni vision'. Proc., 1995 IEEE Int. Conf. on Robotics and Automation, Nagoya, Japan, 1995, vol. 1, pp. 1062–1067

[19] Jechow, A., Kyba, C., Hölker, F.: 'Beyond all-sky: assessing ecological light pollution using multi-spectral full-sphere fisheye lens imaging', *J. Imaging*, 2019, **5**, (4), p. 46. Available at <https://www.mdpi.com/2313-433X/5/4/46>

[20] Sigernes, F., Ivanov, Y., Chernouss, S., *et al.*: 'Hyperspectral all-sky imaging of auroras', *Opt. Exp.*, 2012, **20**, (25), p. 27650

[21] Baker, S., Nayar, S.K.: 'A theory of catadioptric image formation'. Sixth Int. Conf. on Computer Vision, Bombay, India, 1998, pp. 35–42

[22] Onoe, Y., Yamazawa, K., Takemura, H., *et al.*: 'Telepresence by realtime view-dependent image generation from omnidirectional video streams', *Comput. Vis. Image Underst.*, 1998, **71**, (2), pp. 154–165. Available at <https://www.sciencedirect.com/science/article/pii/S1077314298907056>

[23] Bioucas-Dias, J.M., Nascimento, J.M.P.: 'Hyperspectral subspace identification', *IEEE Trans. Geosci. Remote Sens.*, 2008, **46**, (8), pp. 2435–2445

[24] Heinz, D., Chang, C.I., Althouse, M.L.G.: 'Fully constrained least-squares based linear unmixing [hyperspectral image classification]'. IEEE 1999 Int. Geoscience and Remote Sensing Symp., 1999. IGARSS'99 Proc., Hamburg, Germany, 1999, vol. 2, pp. 1401–1403

[25] Heinz, D.C., Chang, C.-I.: 'Fully constrained least squares linear spectral mixture analysis method for material quantification in hyperspectral imagery', *IEEE Trans. Geosci. Remote Sens.*, 2001, **39**, (3), pp. 529–545

[26] Chang, C.I., Heinz, D.C.: 'Constrained subpixel target detection for remotely sensed imagery', *IEEE Trans. Geosci. Remote Sens.*, 2000, **38**, (3), pp. 1144–1159

[27] Settle, J.J., Drake, N.A.: 'Linear mixing and the estimation of ground cover proportions', *Int. J. Remote Sens.*, 1993, **14**, (6), pp. 1159–1177

[28] Bro, R., De Jong, S.: 'A fast non-negativity-constrained least squares algorithm', *J. Chemom.*, 1997, **11**, (5), pp. 393–401

[29] Bioucas-Dias, J.M., Plaza, A., Dobigeon, N., *et al.*: 'Hyperspectral unmixing overview: geometrical, statistical, and sparse regression-based approaches', *IEEE J. Sel. Top. Appl. Earth Obs. Remote Sens.*, 2012, **5**, (2), pp. 354–379. Available at <http://ieeexplore.ieee.org/document/6200362/>

[30] Zhang, X., Sun, Y., Zhang, J., *et al.*: 'Hyperspectral unmixing via deep convolutional neural networks', *IEEE Geosci. Remote Sens. Lett.*, 2018, **15**, (11), pp. 1755–1759. Available at <https://ieeexplore.ieee.org/document/8432512/>

[31] Boardman, J.W.: 'Automating spectral unmixing of AVIRIS data using convex geometry concepts'. Summaries of the 4th Annual JPL Air-borne Geosciences Workshop, Pasadena, 1993, pp. 11–14

[32] Winter, M.E.: 'N-FINDR: an algorithm for fast autonomous spectral endmember determination in hyperspectral data'. SPIE's Int. Symp. on Optical Science, Engineering, and Instrumentation, Denver, CO, USA., 1999, pp. 266–275

[33] Nascimento, J.M.P., Dias, J.M.B.: 'Vertex component analysis: a fast algorithm to unmix hyperspectral data', *IEEE Trans. Geosci. Remote Sens.*, 2005, **43**, (4), pp. 898–910

[34] Xu, X., Tong, X., Plaza, A., *et al.*: 'A new spectral-spatial sub-pixel mapping model for remotely sensed hyperspectral imagery', *IEEE Trans. Geosci. Remote Sens.*, 2018, **56**, (11), pp. 6763–6778. Available at <https://ieeexplore.ieee.org/document/8410597/>

[35] Yan, Y., Hua, W., Liu, X., *et al.*: 'Spatial-spectral preprocessing for spectral unmixing', *Int. J. Remote Sens.*, 2019, **40**, (4), pp. 1357–1373. Available at <https://www.tandfonline.com/doi/full/10.1080/01431161.2018.1524590>

[36] Martin, G., Plaza, A.: 'Region-based spatial preprocessing for endmember extraction and spectral unmixing', *IEEE Geosci. Remote Sens. Lett.*, 2011, **8**, (4), pp. 745–749

[37] Zortea, M., Plaza, A.: 'Spatial preprocessing for endmember extraction', *IEEE Trans. Geosci. Remote Sens.*, 2009, **47**, (8), pp. 2679–2693

[38] Plaza, A., Martinez, P., Perez, R., *et al.*: 'Spatial/spectral endmember extraction by multidimensional morphological operations', *IEEE Trans. Geosci. Remote Sens.*, 2002, **40**, (9), pp. 2025–2041

[39] Martin, G., Plaza, A.: 'Spatial-spectral preprocessing prior to endmember identification and unmixing of remotely sensed hyperspectral data', *IEEE J. Sel. Top. Appl. Earth Obs. Remote Sens.*, 2012, **5**, (2), pp. 380–395

[40] Richards, J.A., Jia, X.: 'Remote sensing digital image analysis: an introduction' (Springer-Verlag Berlin Heidelberg, Berlin, Germany, 2006)

[41] Somers, B., Zortea, M., Plaza, A., *et al.*: 'Automated extraction of image-based endmember bundles for improved spectral unmixing', *IEEE J. Sel. Top. Appl. Earth Obs. Remote Sens.*, 2012, **5**, (2), pp. 396–408

[42] Goenaga, M.A., Torres-Madroneo, M.C., Velez-Reyes, M., *et al.*: 'Unmixing analysis of a time series of Hyperion images over the Guánica dry forest in Puerto Rico', *IEEE J. Sel. Topi. Appl. Earth Obs. Remote Sens.*, 2013, **6**, (2), pp. 329–338

[43] Roberts, D.A., Gardner, M., Church, R., *et al.*: 'Mapping chaparral in the Santa Monica Mountains using multiple endmember spectral mixture models', *Remote Sens. Environ.*, 1998, **65**, (3), pp. 267–279

[44] Degerickx, J., Roberts, D.A., Somers, B.: 'Enhancing the performance of multiple endmember spectral mixture analysis (MESMA) for urban land cover mapping using airborne lidar data and band selection', *Remote Sens. Environ.*, 2019, **221**, pp. 260–273. Available at <https://www.sciencedirect.com/science/article/pii/S0034425718305352>

[45] Lloyd, S.: 'Least squares quantization in PCM', *IEEE Trans. Inf. Theory*, 1982, **28**, (2), pp. 129–137. Available at <http://ieeexplore.ieee.org/document/1056489/>

[46] Baumgardner, M.F., Biehl, L.L., Landgrebe, D.A.: '220 band AVIRIS hyperspectral image data set: June 12, 1992 Indian pine test site 3', 2015. Available at <https://pur.purdue.edu/publications/1947/1>

[47] Jia, S., Qian, Y.: 'Constrained nonnegative matrix factorization for hyperspectral unmixing', *IEEE Trans. Geosci. Remote Sens.*, 2009, **47**, (1), pp. 161–173

## 8 Appendix

See Figs. 22 and 23 (overleaf) for the pseudo codes of the geometrical unmixing algorithms.

---

**Input**  $p, \mathbf{R} \equiv [r_1, r_2, \dots, r_N]$ ,  $num\_skewers$  {  $num\_skewers$  is the number of skewer vectors to project data onto. }

**Output**  $\mathbf{M}$  {  $L \times p$  estimated matrix }

- 1:  $\mathbf{skewers} := \text{randn}(L, num\_skewers)$ ; { normally distributed  $L \times num\_skewers$  samples }
- 2:  $\mathbf{votes} := \text{zeros}(N, 1)$ ;
- 3: **for**  $i := 1$  to  $num\_skewers$  **do**
- 4:    $\text{vol\_aux} := \mathbf{skewers}_{:,i} \mathbf{R}_0$ ; {  $\mathbf{R}_0$  is the zero-mean of  $\mathbf{R}$  }
- 5:    $\text{vol\_aux} := \text{abs}(\text{vol\_aux})$ ;
- 6:    $[\text{max\_vol}, \text{idx}] := \text{max}(\text{vol\_aux})$ ; {  $\text{idx}$  is the indice of the data extreme }
- 7:    $[\mathbf{votes}]_{\text{idx}} := [\mathbf{votes}]_{\text{idx}} + 1$ ;
- 8: **end for**
- 9:  $[\text{val\_aux}, \text{indice}] := \text{sort}(\mathbf{votes})$ ; { sortes votes in descending order }
- 10:  $\text{indice} := [\text{indice}]_1 : p$ ;
- 11:  $\mathbf{M} := [\mathbf{R}_0]_{:, \text{indice}}$ ;

---

**Fig. 22** Algorithm 1: PPI algorithm

---

**Input**  $p, \mathbf{R} \equiv [r_1, r_2, \dots, r_N]$

**Output**  $\mathbf{M}$  {  $L \times p$  estimated matrix }

- 1:  $\mathbf{R}_p := \mathbf{U}_p^T \mathbf{R}_0$ ; {  $\mathbf{U}_p$  obtained by SVD, and  $\mathbf{R}_0$  is the zero-mean of  $\mathbf{R}$  }
- 2:  $\text{indice} := \text{randi}(N, p)$ ; { indice is the randomly selected  $p$  points from  $N$  samples }
- 3:  $\mathbf{R}_{aux} := [\mathbf{R}_p]_{:, \text{indice}}$ ;
- 4:  $\text{max\_vol} := \text{det}(\mathbf{R}_{aux})$ ;
- 5: **for**  $i := 1$  to  $N$  **do**
- 6:    $\mathbf{r} := [\mathbf{R}_p]_{:, i}$ ;
- 7:   **for**  $j := 1$  to  $p$  **do**
- 8:      $[\mathbf{R}_{aux}]_{:, j} := \mathbf{r}$ ; { temporarily updates the  $j^{\text{th}}$  endmember }
- 9:      $\text{vol\_aux} := \text{det}(\mathbf{R}_{aux})$ ;
- 10:     **if**  $\text{vol\_aux} > \text{max\_vol}$  **then**
- 11:        $\text{max\_vol} := \text{vol\_aux}$ ;
- 12:        $\text{indice}_j := i$ ;
- 13:     **end if**
- 14:   **end for**
- 15: **end for**
- 16:  $\mathbf{M} := \mathbf{U}_p [\mathbf{R}_p]_{:, \text{indice}}$ ;

---

**Fig. 23** Algorithm 2: N-FINDR